Experimental and Simulation Study Results of an Adaptive Video Guidance System

R.T. Schappell* and R.L. Knickerbocker†
Martin Marietta Corporation, Denver, Colo.

Studies relating to stellar-body exploration programs have pointed out the need for an adaptive guidance scheme capable of providing automatic real-time guidance and site selection capability. For the case of a planetary lander, without such guidance, targeting is limited to what are believed to be generally benign areas in order to insure a reasonable landing-success probability. Typically, the Mars Viking lander will be jeopardized by obstacles exceeding 22 cm in diameter. The need is dramatized further by the failures of the Russian Mars landers and the more recent Luna 23 that was damaged on impact. Conversely, the benefits of onboard navigation and real-time selection of a landing site and obstacle avoidance have been demonstrated by the Apollo lunar landings, in which man performed the surface sensing and steering functions. Therefore, an Adaptive Video Guidance System (AVGS) has been developed, breadboarded, and flown on a six-degree-of-freedom simulator. This paper describes the principle of operation, breadboard system hardware, results of a digital simulation, and the results of an experimental feasibility demonstration.

Introduction

SCIENTIFIC site selection and obstacle avoidance have been areas of concern since the inception of the space program whereupon various surface sensing techniques were considered for a variety of proposed lunar and planetary missions. As an example, in 1966 a Walleye missile area correlation tracking system was modified for a planetary application to operate in an edge-repelling mode and tested in the laboratory. However, actual performance of this system did not justify the additional power and weight penalty imposed on the early Mars lander configuration. Further studies were conducted whereupon laser scanners, radar scanners, and other optical devices were considered as discussed by Gansler[1] and Davis.[2] Again, complexity, weight, and cost penalties were prohibitive. Ultimately, a simplified video concept was developed and is the subject of this paper.

Although the Adaptive Video Guidance System (AVGS) is applicable to a number of stellar-body exploration programs, the Viking Mars mission was used as a baseline mission in this research program to arrive at a consistent and realistic set of design requirements and goals. The primary objective of this effort was to design and test a breadboard video guidance system that would demonstrate the capability to select autonomously the least hazardous landing site on a complex scaled three-dimensional planetary-surface model. System feasibility was established by a coordinated physical and digital simulation effort. The approach taken was to 1) establish the reference mission requirements, constraints, and maneuver capability; 2) design the site selection algorithms; 3) breadboard the video data-processing logic and integrate it with an image dissector camera; 4) design and build a physical simulator; 5) integrate and program the PDP-9 scientific computer to deive the physical simulator to simulate flights to the surface; 6) build a scaled three-dimensional Mars surface model to be used as the target; 7) check out and calibrate the total integrated system; and 8) run a Monte Carlo simulation consisting of repeated flights to the surface from arbitrary starting positions and altitudes.

Presented as Paper 75-1094 at the AIAA Guidance and Control Conference, Boston, Mass., Aug. 20-22, 1975; submitted Sept. 9, 1975; revision received March 12, 1976. This work was supported by NASA Contract NAS1-13558.

Index category: Spacecraft Navigation, Guidance, and Flight-Path Control Systems.

*Senior Staff Engineer. Member AIAA.

†Senior Engineer.

A digital computer program simulation analysis was performed using a detailed model of the Viking spacecraft terminal descent subsystems along with the AVGS sensor model and a surface model. This analysis provided insight into sensor system parameters and established the feasibility of the system for a Mars-type mission.

Feasibility was based on the system's ability to locate the most acceptable landing site repeatedly in arbitrary areas regardless of initial conditions. The techniques employed, hardware and software implemented, physical simulator characteristics, and experimental results are discussed in the following paragraphs.

Theory of Operation

The AVGS is a unique approach to increasing the probability of a successful landing on an undefined surface. It therefore will contribute significantly to the adaptive capability of a spacecraft targeted to a solar body. The primary ingredients of the AVGS are a TV camera sensor and the processing electronics that operate on raw video data and output a steering bias to the lander computer. The uniqueness of this approach is in the video signal processing logic, which is simple in design and makes maximum use of the available data.

In the case of a planetary lander application, such as the Viking Mars mission, the AVGS would be activated after having jettisoned the parachute and would continue to function during the terminal descent phase. At approximately 1000 m, the system is activated and dynamically scans the area surrounding the predicted impact point (PIP) as determined by the lander computer. The video data then are processed, resulting in a steering command to the lander computer and, consequently, to the propulsion subsystem to avoid rocks, craters, and major slopes, as shown in Fig. 1. The PIP is always within the total-field-of-view (TFV) capability of the AVGS. The TFV is necessarily large to permit observing the PIP in spite of anticipated vehicle attitude excursions necessary for maneuvering during the terminal landing phase. Use of electronic beam positioning obviates the need for extensive data processing of the entire area, for mechanical gimbals, and for reorienting the vehicle to observe the area about the PIP. The scanned field of view (SFV) is a fixed angle, and the surface area scanned diminishes as a function of altitude while resolution improves. The logic permits observation and avoidance of major surface features at higher altitudes where maximum maneuvering capability can be achieved with

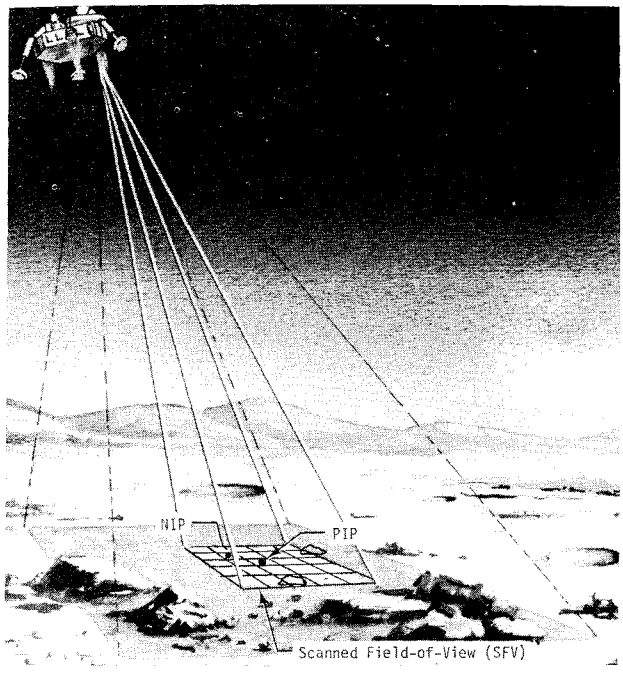

Fig. 1 System operation

minimum fuel consumption. After the AVGS scans the surface, the video data are processed, and a new impact point is selected (the area with the least contrast). A bias steering command to the lander computer initiates maneuvering to the preferred landing site. The sequence is repeated at intervals on the order of 1 sec down to approximately 15 m from the surface. Operating time varies from 20 to 35 sec as a function of propulsion system constraints, control system philosophy, atmospheric density, wind velocity, and maneuvering distance requirements.

The site selection algorithm is implemented in the following manner. Receiving a positioning command from the lander computer, the scanned field of view is centered about this point, and a matrix of A_{ij} areas is scanned, as shown in Fig. 2. Scanning of the A_{ij} subframes is accomplished by biasing the scanning signals to move the scanned area on the photocathode of each of the A_{ij} areas. Typically, each subframe is scanned sequentially with 100 lines and 100 picture elements per line. The video signal then is processed by the appropriate filters.

A 30-kHz low-pass filter is used to remove noise at frequencies above the resolution limit of the camera. The second low-pass 20-kHz filter has its output proportional to the dc component of the video signal. The three output signals, V_L, V_H, and V_M, represent the rectified integral of the dc component, the high-frequency ac components, and the low- to middle-frequency ac components of the video signal, respectively. These outputs then are used in the calculation of the "suitability rating" for each subframe. The rating scheme is as follows:

rating

$$= a\left(\frac{|\bar{V}_M|}{|\bar{V}_L|}\right) + \left(\frac{|\bar{V}_H|}{|\bar{V}_L|}\right)$$

where $|\bar{V}_M|$, $|\bar{V}_H|$, and $|\bar{V}_L|$ are the absolute values of average values of V_M, V_H, and V_L for a subframe. The weighting factor a was selected empirically to give the best agreement between the algorithm and the experimenter's subjective evaluation of various areas. The ratings for the A_{ij} subframes then are compared, and the one with the lowest rating is selected as the new impact point.

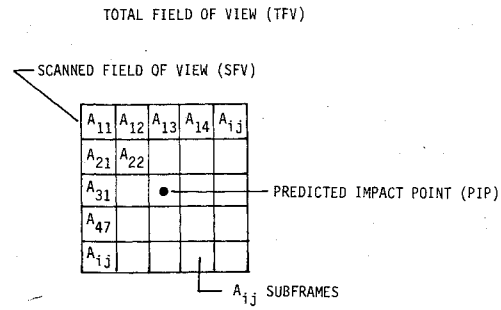

Fig. 2 Scan format.

Laboratory System

The AVGS was breadboarded and evaluated experimentally on a six-degree-of-freedom simulator, which was constructed to support development of the video guidance technology. The simulator consists of four major subsystems: simulator carriage, control console, computer, and surface model. The simulator carriage contains three translational axes and the attitude gimbal assembly. The camera head and a motorized zoom lens are housed in this gimbal assembly, which provides pitch, yaw, and roll angular freedom. The zoom lens provides a 10-to-1 range that is used to simulate large altitude variations in conjunction with the vertical translational axis. Iris and focus control also are achieved via motor drives on this lens.

The control console contains the TV monitor, control panel, digital voltmeter, three bandpass filters, and the site-selection system breadboard electronics. The control panel includes manual controls for the carriage and zoom lens, servo power controls, and mode controls for selecting automatic or manual operation of the simulator. The Digital Equipment Corporation PDP-9 digital computer is an integral part of the video guidance lander (VGL) simulator in that it facilitates rapid evaluation of a new processing algorithm; it is essential for automating the experiments by driving the simular axis and commanding altitude via the zoom lens servo.

Because of its adaptive sensing ability, photometric output, and controllable scan, an image dissector camera system was used in performing the experiments. Basically, it is a photomultiplier with a small, electrically movable photocathode area. An electron lens accelerates and focuses all electrons emitted from each point (or small area) in the plane of a dissecting aperture. The resulting electron image, which is a direct measure of the optical input radiation pattern, then is deflected electronically across the aperture. The aperture, consequently, samples the photocathode at any instant of time. Following the aperture, the sampled photoelectrons are multiplied in an electron multiplier by a large factor (commonly 10^5 or 10^7) and emerge as a current in the output anode circuit. Therefore, the detector output is a direct function of the light flux incident on the photocathode (image plane) and hence is a direct function of the illumination from the projected sample area on the surface. These subsystems are integrated as shown in Fig. 3, and, as can be seen, remote control is provided for the iris, focus, zoom, and field-of-view segment.

The surface simulation model used in the feasibility demonstration consisted of a 2.5-m-diameter octagonal box filled with 10 cm of lunar nominal NASA-furnished material. Geomorphological variations were implemented at a 300:1 scale by formation of craters, channels and channel outlets, volcanic structures, dunes, ripples, and knolls. Multiple variations in the surface granularity were accomplished by screening the model material to control obstacle distribution and affect albedo variations.

Experimental Results

Having breadboarded the AVGS, it was calibrated optically by conducting experiments designed to characterize actual

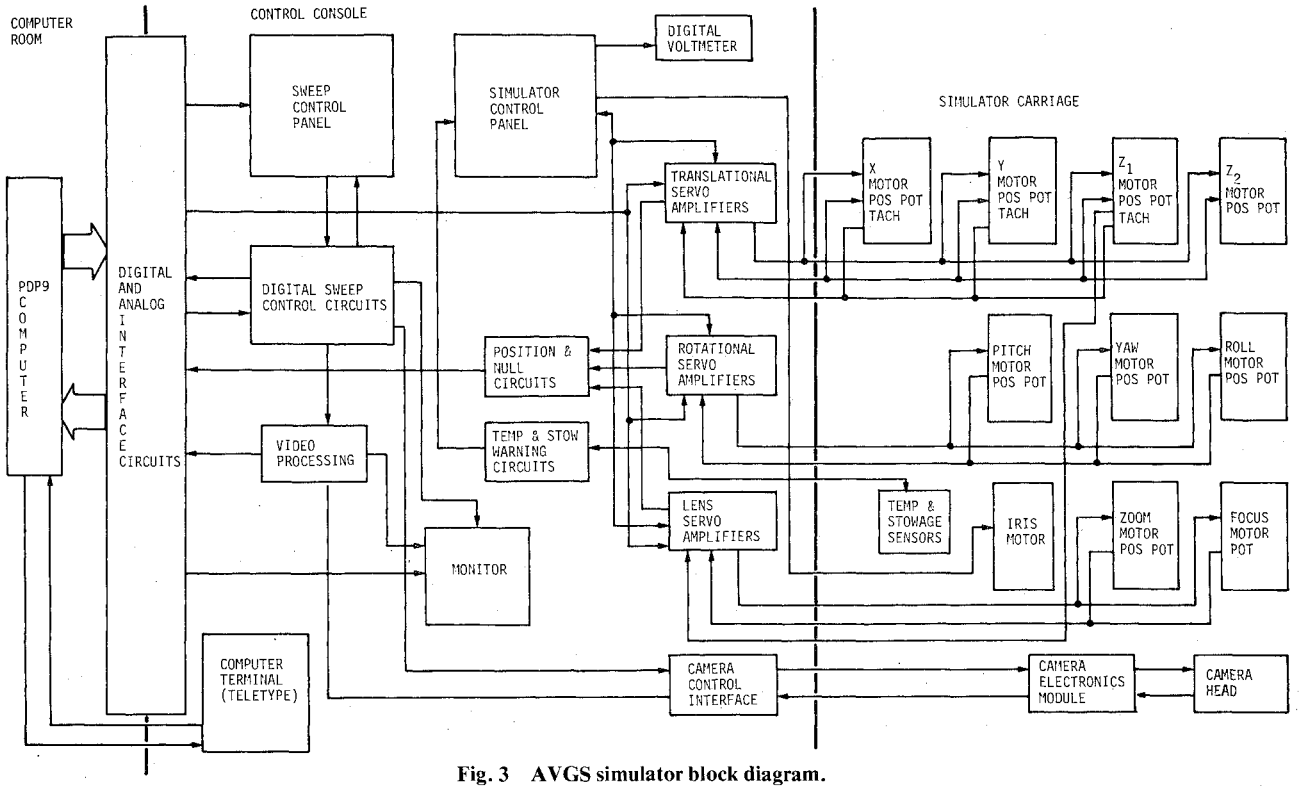

Fig. 3 AVGS simulator block diagram.

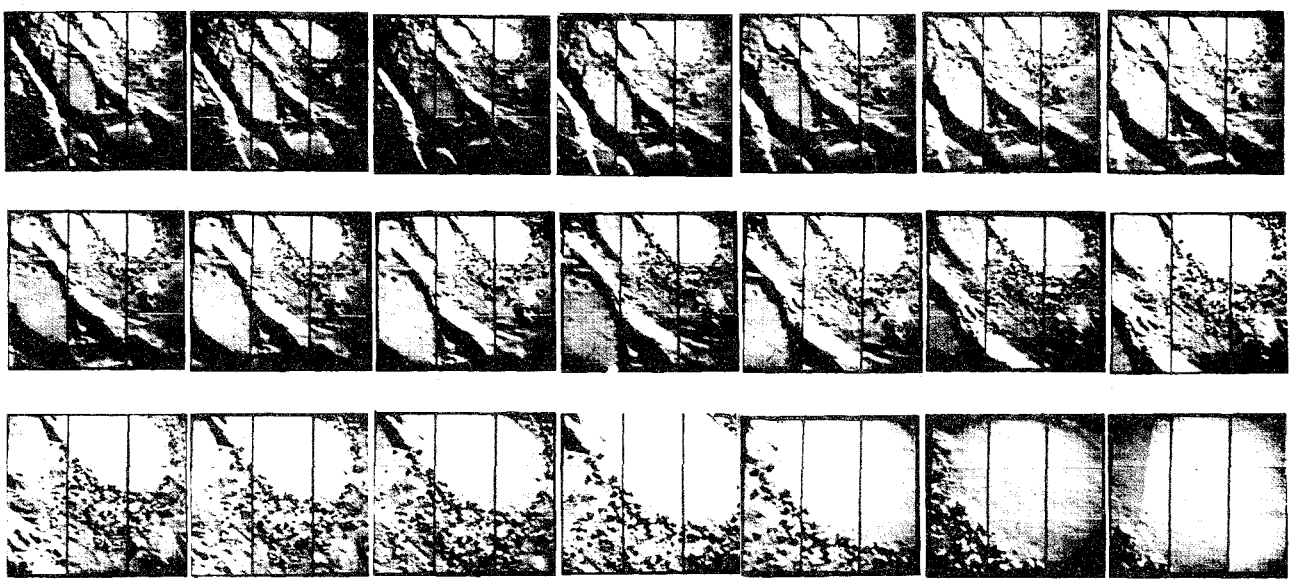

Fig. 4 Monitor observations for a typical experiment.

system performance. As an example, the modulation transfer function was derived experimentally as a function of the spatial frequency of information in the scene viewed by the cameras. These experiments resulted in an estimate of the system's ability to "see" a given target. Having calibrated the system, the algorithm evaluation experiments were performed to establish site-selection feasibility. In performing these experiments, consideration was given to spectral band selection, weighting factors, altitude vs resolution effects, combining of filtered outputs, and scan mechanization.

The first approach considered was a time-domain technique in which each ac component was monitored to determine the amount of time the voltage was above a threshold compared to the amount of time it was below the threshold, as discussed in Ref. 3. Under near-ideal lighting conditions, the approach worked well with fairly simple hardware; but when lighting variations were introduced on a three-dimensional model, the ratings did not always correlate well with site desirability. When methods for reducing sensitivity to lighting were considered, the required hardware became significantly complex; therefore, the approach was modified.

When a camera with a linearly responding photocathode is used, the ratio of ac component in the video signal to dc component is approximately constant for a given scene over an "illumination" range of more than 4 to 1. The ratio of the ac-to-dc voltage output then would provide an index of surface roughness which is independent of scene brightness. This is the approach used in the following experiments.

Experiments were conducted to determine what frequency ranges best distinguished high-contrast targets from low-contrast targets as defined by Schappell et al.[4] Preliminary results indicated that certain rough areas were best

distinguished from others in the bands from 30 Hz through 9 kHz and from 1 through 30 kHz. These bands were, therefore, used in the experiments. The ac components of the signal were measured with circuits that respond to average absolute value because of the circuit simplicity. Therefore, the figure of merit (FOM) was derived in the following manner

$$\text{FOM} = a\left(\frac{|\bar{V}_M| - b}{|\bar{V}_L| - c}\right) + \left(\frac{|\bar{V}_H| - d}{|\bar{V}_L| - e}\right)$$

where $|V_M|$, $|V_H|$, and $|V_L|$ are the midband, high-band, and dc-component average absolute values. The constants *b, c, d,* and *e* were introduced to correct for noise and offset voltages so that the ratio would be constant for a given scene regardless of light level due to laboratory limitations.

Figure 4 illustrates actual experimental results using this algorithm and a 3×3 subframe scan. This sequence of pictures was taken from the console television monitor. In actual operation, the nine subframes were scanned sequentially. After each scanning sequence of nine areas, the area with the least amount of contrast was selected as the desired landing site. The final site (the center of the last photograph) was the result of 20 observations and decisions.

The next series of experiments involved a Monte Carlo approach in which the system computer was programmed to select an initial simulated altitude between 500 and 900 m and an initial *X, Y* position above the three-dimensional Martian surface model at random using a random number generator. It then calculated altitudes and predicted impact points for the lander as it approached the surface under system guidance. The computer received guidance information 20 times during the descent. When the simulated altitude reached 100 m, the predicted impact point was recorded on tape. Fifty of the landing sites selected during a typical Monte Carlo run are indicated by the small ovals in Fig. 5.

To provide a comparison for estimating success probability, unguided simulated landings also were run. The total experiment was automated and set up in a manner that eliminated experimenter bias through the use of several additional experimenters. The results obtained from the initial preliminary experiments indicated that, without the AVGS logic in an unguided situation, 9 out of 48 landings would have been successful, but, with the AVGS logic in a guided situation, 47 out of 50 would have been successful. Furthermore, in the guided mode, the system always avoided extremely rough sites even though initial position and altitude did not provide a field of view with a distinctly smooth area. For these experiments, sun angle was 60° from normal to the surface, and the guidance mode limited the landing site to the area defined during the first high-altitude observation.

Digital Simulation

Digital simulation analysis was performed to evaluate the feasibility of a specific implementation of the site selection system. The Viking mission and vehicle were used for this analysis. Functions required for the site selection system were modeled and added to MOD6MV, an existing digital computer program. MOD6MV is a modularized six-degree-of-freedom program that was developed by Stafford et al.[5] and used as a design tool for Viking. It can simulate all phases of the mission; however, only the terminal descent phase was simulated for this analysis. The site selection simulation required the addition of a surface model, a sensor model, impact prediction, and a steering algorithm, which are discussed in the following paragraphs. The results obtained from this digital simulation are quite credible because of the proven authenticity of MOD6MV and the realism of the surface and AVGS sensor model.

Surface Model

The surface model was constructed before the terminal descent simulation. The surface consists of a 500×500 grid of

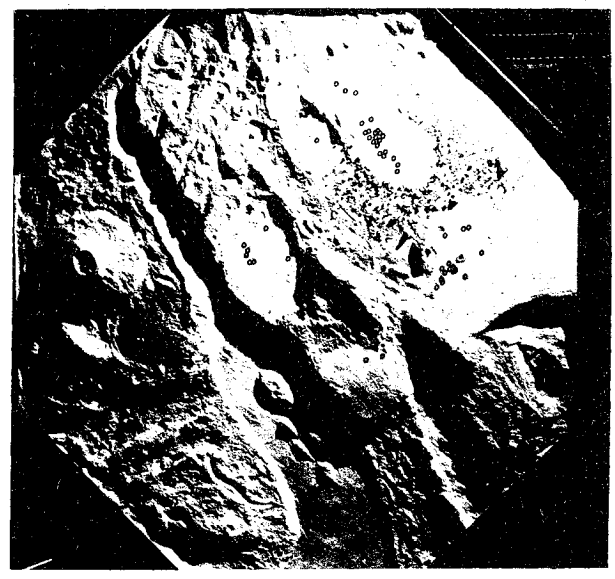

Fig. 5 Monte Carlo simulation results.

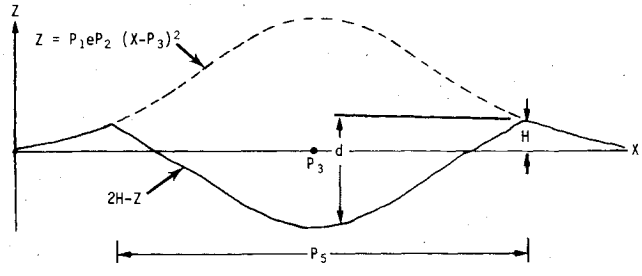

Fig. 6 Cross section of crater function.

gray levels ranging from 0 (light) to 7 (dark), representing the amount of light reflected to the sensor from discrete points of a set of functions defining various surface features. The amount of light received at the sensor from an incremental area of the surface depends on many factors; however, only the angle θ between the surface normal and the sun line need be considered. Then,

$$F = \cos\theta \tag{1}$$

yields a number proportional to the light intensity received at the sensor from each point on the surface. The values of F are scaled from the range 0 to 1 to the range 7 to 0 and quantized. This measure of reflected light plus the knowledge of shadow positions make it possible to create a realistic model of the surface.

Simple three-dimensional mathematical functions were determined to represent a variety of surface features. The function used to represent a crater is

$$Z = P_1 \exp\{P_2[(X-P_3)^2 + (Y-P_4)^2]\}\ P_1>0,\ P_2<0 \tag{2}$$

Assume that the crater has diameter P_5, rim height H, and depth d. H and d are used to determine the values of P_1 and P_2. The crater elevation takes the value z for points $(x)y)$ outside a circle centered at (P_3, P_4) with diameter P_5. Inside this circle, the crater elevation is given by $2H-z$ (see Fig. 6).

The function used to represent a rill is

$$z = P_1 \exp\{P_2[P_3x + P_4 - y] - P_5\}\ P_1,\ P_2<0,\ P_5>0 \tag{3}$$

The rill has depth P_1 and runs along the line $y = P_3x + P_4$. The parameters P_2 and P_5 control the slope and shape of the rill sides. Boulders of varying sizes are represented by spheres.

The gray level at each point for a fixed sun position now can be determined by using the surface elevation to determine shadow positions and by using the derivative of the functions to calculate a vector normal to the surface to establish the amount of light reflected. Implicit three-dimensional data now are available for processing by the sensor. The surface is illustrated in Fig. 7. This figure was produced by using the CDC 280 plot package to fill in a small box at each grid point with lines so that the ratio of light to dark area is proportional to the gray level for that point. The surface is accessed by defining a mapping that takes a point (I, J) of the grid to a point in planet-centered inertial coordinates. It is necessary to define the distance between grid points and to reference the grid to a point in planet-centered inertial coordinates. When the desired coordinates of the center of the sensor scan area are known, it then is possible to retrieve the correct surface data for processing.

Sensor Model

The sensor model is designed to simulate functionally the operation of an electro-optical sensor by collecting the gray-level surface data, processing them, and performing obstacle avoidance. A 3×3 subframe scan is used. Sensor operation for each scan begins with a pointing command. The initial surface scan is centered at the lander's predicted impact point. Subsequent scan positions are determined by the most recent landing-site choice. The scan is positioned so that the coordinates of the center of the subframe chosen during the last scan are the coordinates of the center of the corresponding subframe for the next scan. For example, if the first two decisions chose the upper right subframe as the best area, the scan positioning would be shown in Fig. 8. Note that the coordinates of the center of the upper right subframe remain constant.

Video data collection is simulated using the gray levels from the surface model and taking the sensor ground resolution into account. Assume that the sensor is scanning an area consisting of $n\times n$ grid points with a distance d between points and that the sensor has ground resolution r with $r>d$. The scanned area of $n\times n$ grid points is transformed to $(nd/r)\times(nd/r)$ points, where each point is the average gray level of r^2/d^2 points. For example, assume that the scanned area is 12×12, with a 0.914-m spacing between points, and that the sensor's ground resolution is 828 m. Then the information actually collected by the sensor is represented by 6×6 grid points, where each point is the average of four points from the actual surface data (see Fig. 9).

The figure-of-merit calculation for a subframe is performed by averaging the gray levels for that subframe and then summing the absolute differences between this average and the gray level at each point. The resolvable gray levels are used for these calculations. This provides a realistic measure of contrast for the subframe and functionally simulates the process of removing the dc component of a video signal, rectifying the ac portion, and integrating. A large figure of merit corresponds to high contrast.

After the nine areas are scanned and the figures of merit are calculated, the desired landing site is chosen. This choice is not based on the minimum figure of merit, as in the laboratory experiments, but is based on a negative gradient direction indicating decreasing contrast. The sums of the figures of merit are computed for each row and each column of the 3×3 area. The area chosen as the most desirable landing site is the one that is in both the lowest contrast row and the lowest contrast column. This scheme prevents the sensor from choosing a smooth area surrounded by very rough areas.

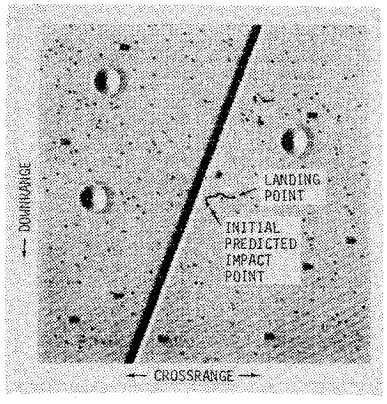

Fig. 7 Plot of predicted impact point.

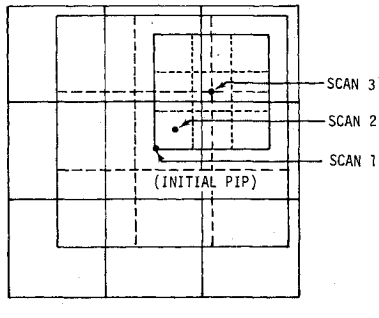

Fig. 8 Scan positioning scheme.

Impact Prediction

Calculation of the lander's predicted impact point is required for initial sensor pointing commands and determination of steering commands. The impact coordinates are calculated by integrating numerically a set of equations (derived from the equation of motion) and by making certain simplifying assumptions for the so-called "gravity turn" that is executed by the terminal descent guidance and control system. Simplified equations of motion for the gravity turn, where the vehicle thrust vector is assumed opposite the velocity vector, are

$$dV/dt=a+g\cos\psi \tag{4}$$

$$V(d\psi/dt)=-g\sin\psi \tag{5}$$

$$dH/dt=-V\cos\psi \tag{6}$$

where

t = time, V = magnitude of velocity vector, a = vehicle acceleration, g = gravitational acceleration, ψ = angle between velocity vector and local vertical and H = altitude. The downrange distance is determined by

$$dR/dt=V\sin\psi \tag{7}$$

where R is the downrange distance.

These equations are integrated numerically until the vehicle enters the constant-velocity phase, which produces zero additional downrange distance because of near-vertical descent. The trajectory obtained from this prediction routine is shown in Fig. 10, together with the actual trajectory flown. This prediction occurred at the highest altitude for this simulation and represents a worst-case error because prediction accuracy increases as altitude decreases. Impact prediction is repeated for each scan, at 1-sec intervals during the descent.

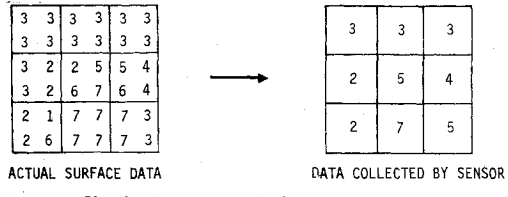

Fig. 9 Sensor resolution simulation.

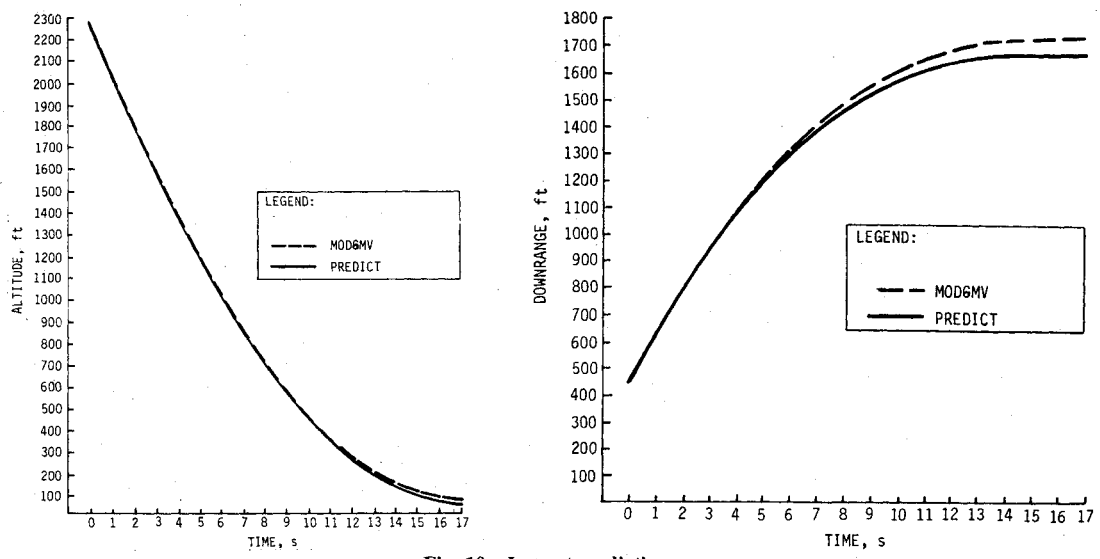

Fig. 10 Impact prediction.

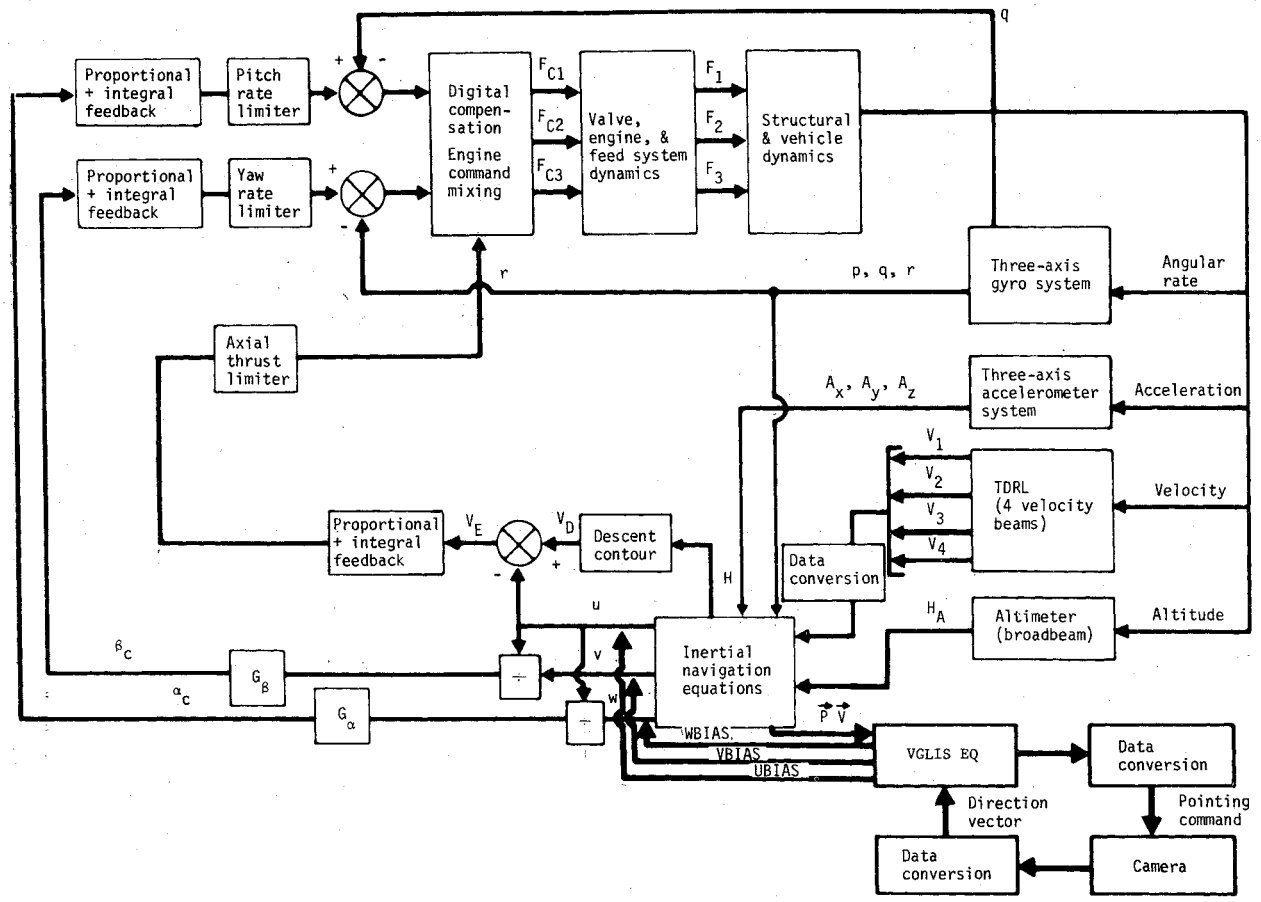

Fig. 11 Viking terminal descent simulation program block diagram.

Guidance

The Viking lander follows a preprogrammed velocity-altitude descent contour to the surface during the powered portion of flight. Steering is accomplished by providing an additional bias velocity vector to translate the predicted impact point from that obtained by following the descent contour to the point chosen by the sensor. A vector velocity function decreasing linearly to zero is calculated based on the desired maneuver distance and the time remaining until impact. The bias velocities must go to zero in order to assure a safe landing.

This steering implementation causes the vehicle to depart slightly from the gravity turn. The thrust vector is no longer pointed opposite the velocity vector, and therefore propulsion efficiency is reduced slightly. This requires some additional fuel and suggests that the descent contour be designed with additional throttle margin.

System Integration

The position and velocity of the lander, available from the flight computer, are used to predict the impact point for initial sensor pointing and determining steering commands.

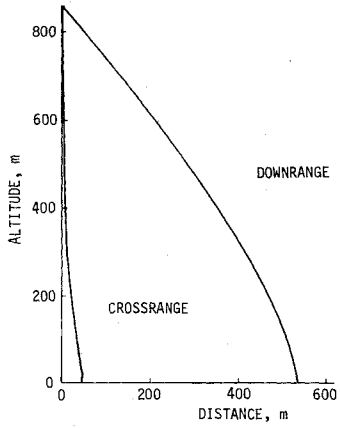

Fig. 12 Plot of trajectory crossrange and downrange.

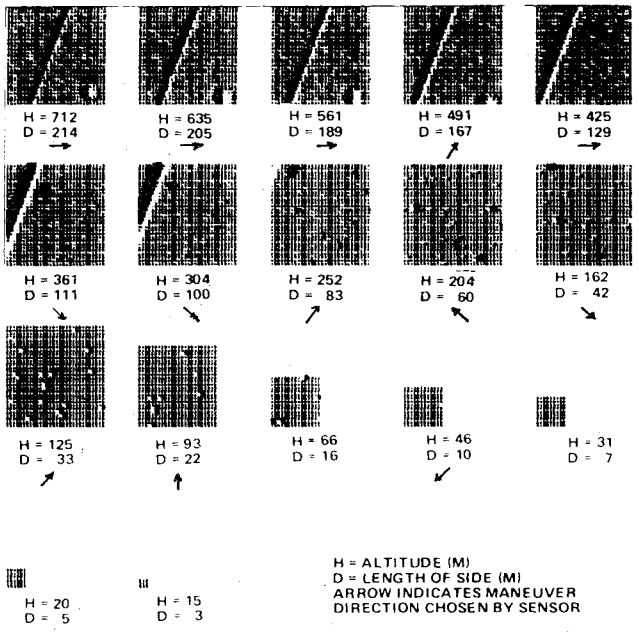

Fig. 13 Site selection sensor simulation.

After scanning the surface, a site is selected, and the bias velocity vector for steering is calculated and fed to the navigation system, as shown in Fig. 11.

Simulation Results

A number of landings were made on the surface illustrated in Fig. 7, all successfully avoiding obstacles. This surface represents a 460- ×460-m area containing one 27-m rill, four 37-m craters, 20 7-m craters, 10 7-m boulders, 282 3-m boulders, and 4729 22-cm rocks. This surface differs from the model used in the laboratory in that there are no distinctly superior areas in which to land.

The predicted impact point for one of the landings is plotted on the surface to show how the landing site changes during descent. Crossrange and downrange views of the trajectory are shown in Fig. 12. Note that this particular landing required primarily a crossrange maneuver. This landing simulation is for maximum-velocity initial conditions requiring maximum fuel consumption. This represents a worst-case performance requirement for the propulsion and guidance system. The surface, as seen by the sensor during the landing, is shown in Fig. 13. The lander altitude and the length of a side of the scanned area also are shown. The arrow underneath the field of view indicates which of the nine subframes was chosen by the sensor. The absence of an arrow indicates that the center subframe has been chosen. The sensor avoids the major obstacles at the higher altitude. When the ground resolution is adequate, it senses and avoids the smaller rocks, finally landing in an area that is completely smooth.

Additional analysis was performed to determine fuel requirements for flying to any point within the original field of view. Maximum additional requirement of 3.4 lb above the nominal consumption of 126.5 lb was established. The digital simulation established the feasibility of adding a site selection sensor system to a Viking-type spacecraft.

Summary

During future development of the AVGS, further consideration will be given to vehicle control and maneuvering logic, since oscillation between two equally acceptable landing sites is not desirable. Furthermore, additional experimental work is planned with regard to field-of-view, resolution, photocathode characteristics, scan format, and optimum frequency filter bandwidth selection. This then will culminate in the selection of the most suitable imaging devices for a given mission.

Analytical and experimental results acquired to date indicate that a relatively simple system of this type could increase greatly the probability of mission success for unmanned planetary landers where Earth control is not practical. It could enhance significantly science return by allowing targeting of geomorphologically complex sites on planets and asteroids and provide a truly adaptive capability for a solar-body explorer. Other uses, such as entry guidance, scientific imaging, scientific site selection, and Earth orbital pointing and tracking are being stuided and will certainly be essential for future spacecraft programs.

References

[1]Gansler, J. S. and Bomzer, H. W., "Lunar and Planetary Terminal Point Guidance Using an Optical Correlator," *Proceedings of Astrodynamics Guidance and Control, XVIIth International Astronautical Congress, 1967,* Madrid, Spain, 1966, pp. 257-264.

[2]Davis, L. S., "A Survey of Edge Detection Techniques," Rept. NSF-OCA-GJ32258X-24, Nov. 1973, Maryland Univ., College Park, Md.

[3]Schappell, R. T. and Johnson, G. R., "Experimental and Simulation Study Results of a Planetary Landing Site Selection System," *Journal of Spacecraft and Rockets*, Vol. 10, April 1973, pp. 277-280.

[4]Schappell, R. T., Knickerbocker, R. L., Tietz, J. C., Grant, C., and Flemming, J. C., "Video Guidance, Landing, and Imaging Systems for Space Missions," Final Rept., NASA CR-132574, Feb. 1975.

[5]Stafford, P. S., et al., "MOD6MV Simulator Program Terminal Descent Users Guide," NASA CR-22-69-16, July 1969.